J Nanopart Res (2017) 19: 166
DOI 10.1007/s11051-017-3858-y

RESEARCH PAPER

Highly Stable Hierarchical Flower-like β-In_2S_3 Assembled from 2D Nanosheets with high Adsorption-Photodecolorization Activities for the Treatment of Wastewater

Yang Cheng · Helin Niu · Jingshuai Chen · Jiming Song · Changjie Mao · Shengyi Zhang · Changle Chen · Yuanhao Gao

Received: 9 December 2016 / Accepted: 11 April 2017 / Published online: 3 May 2017

Abstract The hierarchical flower-like β-In_2S_3 catalyst assembled from 2D nanosheets was prepared using an organic-component depletion method utilizing inorganic-organic hybrids indium diethyldithiocarbamate (In-DDTC) as a single-source precursor. The crystallization, morphology and composition of the as-synthesized β-In_2S_3 were characterized by XRD, SEM, TEM, EDS and XPS, respectively. The β-In_2S_3 possessed high specific surface area of 134.1 m^2 g^{-1}, adsorption capacity of 195.5 mg g^{-1} for methylene blue, and extreme photodecolorization speed under visible light irradiation for the complete removal of methyl orange (MO) dye within 15 min and tetracycline within 60 min. Although methyl orange concentration decreased quickly, the total organic carbon (TOC) decreased slowly. UV-vis and mass spectrometry (MS) were applied to analyze the intermediates coming from the photodecolorization of MO. In order to estimate the roles of active species during the decolorization of MO, trapping experiments were conducted to determine the main active species during the decolorization process. The results indicated that $\cdot O_2^-$ radicals and e^{-1} were the key intermediates. This enhanced activity was attributed to its unique structures assembled from 2D nanosheets with thickness of ca. 5-7 nm, leading to high specific surface area, wide range of pore size distribution and great efficiency in absorbing light and electron/hole separation. The hierarchical flower-like β-In_2S_3 demonstrated great advantages in the treatment of various wastewater pollutants including textile dyes and antibiotics.

Keywords Single-source precursor · Indium sulfide · Adsorption · Photodecolorization · Wastewater · Two dimensional nanosheets · Nanostructured catalysts · Removal antibiotics from waste

Electronic supplementary material The online version of this article (doi:10.1007/s11051-017-3858-y) contains supplementary material, which is available to authorized users.

Y. Cheng · H. Niu (✉) · J. Chen · J. Song · C. Mao · S. Zhang
Department of Chemistry, Key Laboratory of Functional Inorganic Materials of Anhui Province, Anhui University, Hefei 230039, People's Republic of China
e-mail: niuhelin@ahu.edu.cn

C. Chen
CAS Key Laboratory of Soft Matter Chemistry, Department of Polymer Science and Engineering, University of Science and Technology of China, Hefei 230026, China

Y. Gao
Institute of Surface Micro and Nano Materials, Xuchang University, Henan 461000, China

Introduction

The photocatalytic performance is strongly dependent on the catalyst architectures including geometry, morphology and hierarchical structures (Xiao et al. 2004). Recently, two-dimensional (2D) nanomaterials with characteristics of intrinsic quantum confined electrons and more specific surface areas have gained more and more attention in catalysis (Guo et al. 2015). For

example, ultrathin $C_3N_4/Bi_2O_5I_2$ layered nanojunctions display great photocatalytic activities (Xia et al. 2016). However, these 2D nanomaterials share the common limitations of high tendency to aggregate and restack due to the lack of intrinsic driving force for 2D anisotropic growth (Zhang and Xie 2013). The development of three-dimensional (3D) architectures assembled from 2D nanomaterials is an efficient strategy to cope with this challenge (Wang et al. 2014, 2015). Three-dimensional (3D) structured materials assembled from 2D nanomaterials can combine the advantages of the individual properties of their building blocks as well as the novel characteristics and properties of the secondary architectures (Li et al. 2016; Wu et al. 2013b). For example, they possess porous structures made from their adjacent nano-units, large specific surface area to supply abundant active sites (Liu et al. 2015), cavity-mirror effect to improve optical irradiation and the easy solid/liquid separation (Wu et al. 2013a; Wei et al. 2014), all of which lead to enhanced light-harvesting capacity. For instance, 3D Ni_3S_4 frames have both high free volume and high compressive strength compared to flat Ni_3S_4 sheets (Wang et al. 2015). Graphene sheets crumple into paper ball-like structures to make them aggregation-resistant even after mechanical compression (Luo et al. 2013). To date, metal chalcogenide materials have attracted significant attention in the photocatalysis field due to their low cost and specific optical, acoustic, electronic properties (Liu et al. 2015; Meng et al. 2016). Therefore, the preparation of 3D architectures from the assembly of 2D metal chalcogenide nanomaterials may lead to the formation of high performance photocatalyst (Sun et al. 2016).

As an important class of transition metal chalcogenides, Indium sulfide (In_2S_3) is of great interest due to its simple synthetic procedure, low toxicity, and potential applications in photocatalysis (Nayak et al. 2014). Typically, β-In_2S_3 is n-type semiconductor with defected spinel structure and a band gap of 1.9-2.3 eV (Zhou et al. 2014), making it a great candidate for photocatalytic applications (Nayak et al. 2014). Many efforts have been devoted to synthesize β-In_2S_3 with various architectures: 3D hierarchical-like β-In_2S_3 hollow microspheres (Rengaraj et al. 2011), walnut-like In_2S_3 microspheres (Chai et al. 2012) and β-In_2S_3 nanotubes (Liu et al. 2011) using microwave irradiation (Patra et al. 2006), solvothermal (Chai et al. 2012) and sonochemical (Gorai and Chaudhuri 2005) methods. However, most of the aforementioned processes depend on poisonous organic solvents as the reaction media, various surfactants as templates and highly toxic sulfur sources to control the ions activity (Lee et al. 2005; Du et al. 2008; Abdelhady et al. 2013). For example, the most commonly used sulfur sources for the synthesis of β-In_2S_3 are sulfur powder (Park et al. 2006), sodium sulphide (Chai et al. 2012), and lauryl mercaptan (Liu et al. 2011). Therefore, the development of alternative simple and green method is highly desired. Recently, novel inorganic functional materials are prepared using inorganic-organic hybrids as single-source precursors. This method can combine the superior performance of both inorganic building blocks and organic components. Most importantly, inorganic-organic hybrids can serve as handy and effective precursors to prepare novel materials with good control of different components and the retention of macromorphology (Wu et al. 2015). This single-source precursor route has several appealing features. First of all, it offers the potential advantages of mildness and simplified fabrication procedure and does not need exact control over starting material stoichiometry. Moreover, unusual crystal growth selectivity or metastable phase formation may be achieved, which are sometimes unattainable with the conventional synthetic technique (Zhang et al. 2005). For instance, inorganic hollow $Cd_xZn_{1-x}Se$ nanoframe (Wu et al. 2012), and porous MoS_2 nanotubes (Zhuo et al. 2013b) have been synthesized through an ion-exchange and component stripping strategy using inorganic-organic hybrids.

Herein, we reported a facile hydrothermal strategy to synthesize hierarchical flower-like β-In_2S_3 assembled by 2D thin nanosheets. This is a green synthetic method which distilled water as the only solvent, and does not require post-treatment procedure. The flower-like hierarchical structures were prepared by decomposition of single-source precursor indium diethyldithiocarbamate (In-DDTC). The prepared hierarchical flower-like β-In_2S_3 possessed large surface area, good adsorption performance for cationic dye of methylene blue (MB) and great catalytic properties for the decolorization of methyl orange (MO) and tetracycline (TC). To the best of our knowledge, there have been very few reports on the application of In_2S_3 material as efficient photocatalyst for the removal of antibiotics in wastewater.

Experimental procedure

Materials

Indium nitrate hydrate ($In(NO_3)_3 \cdot xH_2O$) was purchased from Aladdin Industrial Corporation. Sodium diethyldithiocarbamate trihydrate ($C_5H_{10}NNaS_2 \cdot 3H_2O$) and ethyl alcohol were purchased from Sinopharm Chemical Reagent Co. Ltd., and all the analytical reagents were used without further purification.

Synthesis of hierarchical flower-like β-In_2S_3

Synthesis of indium diethyldithiocarbamate complex

In a typical procedure, 0.002 mol $In(NO_3)_3 \cdot xH_2O$ and 0.006 mol sodium diethyldithiocarbamate were dissolved in 40 mL deionized water with agitation. The mixed solution was formed a stable white suspension and stirred for 2 h. The white product was collected by filtration, washed with deionized water and dried in air at 60°C.

Synthesis of hierarchical flower-like β-In_2S_3

Subsequently, a certain amount of the as-prepared single-source precursors were added into a 50 mL PTFE-lined stainless steel autoclave containing 40 mL deionized water, and the pH of the solution was adjusted to 3.0 by adding diluted nitric acid. The autoclave was sealed, maintained at 180°C for 12 h. After cooling to room temperature naturally, the obtained yellow precipitate was centrifuged at 8000 rpm for 5 min, washed with ethanol and deionized water for several times and dried overnight at 60°C. The control experiments were conducted by following similar procedure.

Results and discussion

Crystal structure and morphology

The hierarchical flower-like β-In_2S_3 assembled by 2D nanosheets was yellow powder (inset of Fig. 1a). The crystalline phase and morphology of the In_2S_3 were characterized by XRD, SEM and TEM. The typical XRD pattern of the nanostructures was shown in Fig. 1a. The peaks related to the (440), (211), (311), (400) planes could be indexed as cubic β-In_2S_3 phase by

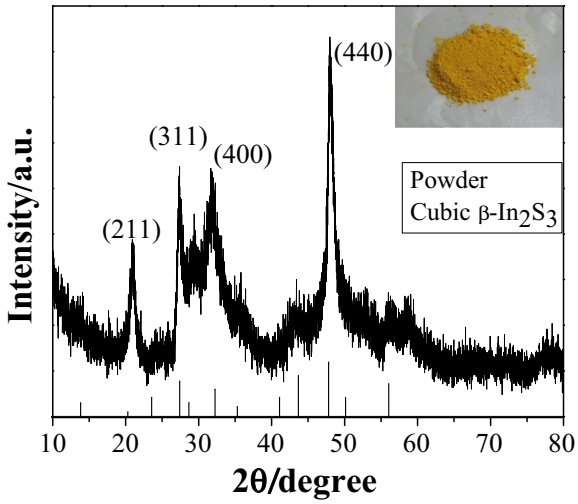

Fig. 1 XRD pattern, inset is the photograph of as-prepared the hierarchical flower-like β-In_2S_3.

careful comparison with JCPDS card file no. 32-0456. No other impurities such as In_2O_3 or $In(OH)_3$ were detected, indicating the high purity the sample, which were consistent with description in the literature (Chen et al. 2008). The powder had low crystallinity, which might show unique physical and chemical properties with more active sites and isotropic nature (Zhang et al. 2015).

The morphology of the as-prepared In_2S_3 was investigated by SEM and TEM. As could be seen in Fig. 2(a-b), the irregular flower-like spherical architectures of In_2S_3 were constructed from many interconnected thin nanosheets with thickness of ca. 5-7 nm. Notably, the flower-like β-In_2S_3 architectures possessed a number of mesoporous, which would help to increase the contact area and accelerate the ion transfer. The more detailed structural information of these hierarchical submicrospheres was revealed via TEM and HRTEM. Fig. 2(c-e) proved that the submicrospheres were built from numerous small thin 2D nanosheets, supporting the SEM analysis (Fig. 2b). The HRTEM image of a single nanosheet (Fig. 2f) revealed that the lattice fringes were perfectly aligned across the surface. The measured interplanar spacing was 0.3101 nm, corresponding well with the (400) plane of cubic In_2S_3.

To better understand the fabrication process for the hierarchical flower-like β-In_2S_3 assembled by 2D thin nanosheets, and time-dependent evolution of morphology at 180°C was elucidated by SEM (Fig. 3a-f). After solvothermal treatment for 2 h, a large amount of prisms appeared, with sizes ranging

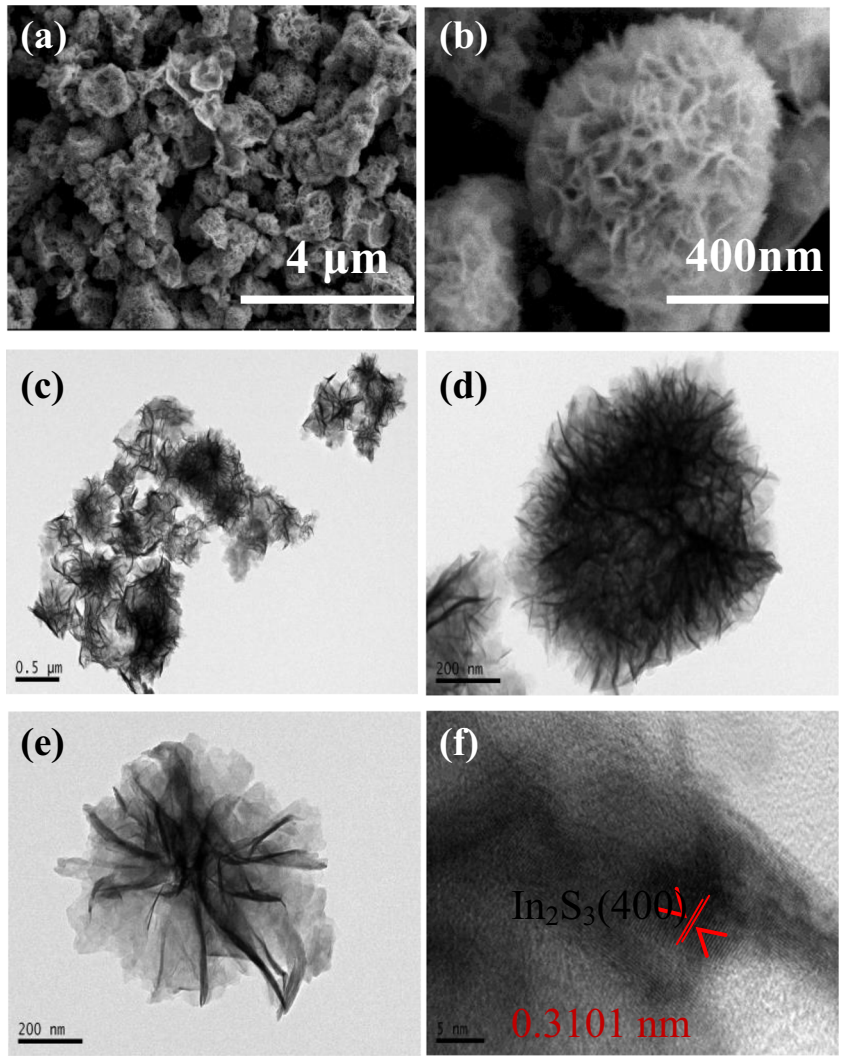

Fig. 2 (a-b) SEM images; (c-e) TEM images; (f) HRTEM image of as-prepared the hierarchical flower-like β-In_2S_3.

from several hundred nanometers to a few micrometres (Fig. 3a). There were also small amounts of particles with curved surface (Fig. 3b). After 4 h, more flower-like hierarchies were formed few larger prisms were observed (Fig. 3c). The surface of large prisms grew coarse, indicating the beginning of the change of morphology. After 6 h, prisms were all already transformed into flowery hierarchies composed of mutual crisscross nanosheets (Fig. 3e). Meanwhile, a solid with folded surface could be found, which might be the intermediate in the process of morphological evolution (Fig. 3f). After 12 h, the submicrospheres were formed from numerous small thin 2D nanosheets, along with some imperfect morphology (Fig. 2a-e). Clearly, this was a gradual, three-stage morphological evolution process: pre-crystallized nuclei and crystal growth of primary particles; oriented attachment of prisms; and Ostwald-ripening of flowery hierarchies (Fig. 3g). At high temperature and vapor pressure, the precursor decomposed and quickly formed pre-crystallized nuclei and crystal growth into prisms. Due to the anisotropic structure of crystal, the prisms further grew into 2D nanosheets through oriented attachment. Furthermore, under longer hydrothermal treatment, large flowery hierarchies might collapse and generate some rupture parts of small flowers. These kinds of flowery hierarchies provided a large active surface area and higher efficiency of incident photons, and leading to higher photocatalytic activity. The final stage for the formation of flower-like structure could be due to

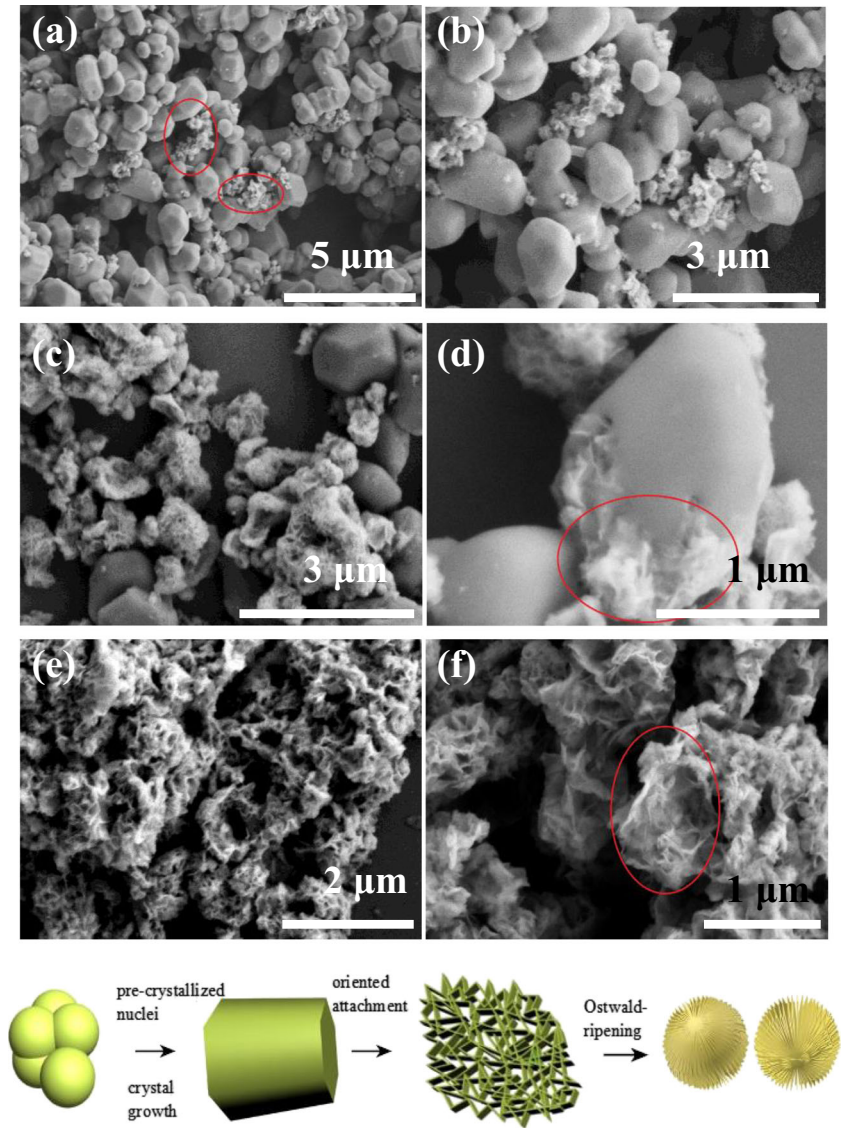

Fig. 3 SEM images of the samples collected at different time period: (a)-(b) 2h; (c)-(d) 4h; (e)-(f) 6h; (g) Schematic illustration of the formation mechanism of the flower-like structure.

the Ostwald ripening. The more accurate formation mechanism is currently under investigation.

Composition and chemical states

EDX analysis was performed on the as-prepared hierarchical flower-like β-In_2S_3 to identify the elements present and measure their composition. The EDX spectrum (Fig. 4a) confirmed that there was no element other than In and S presented in the sample. The chemical state of the as-synthesized sample was further characterized by XPS analysis. The typical survey spectrum of the hierarchical flower-like β-In_2S_3 was shown in Fig. 4b. It revealed that no peaks of other elements except In, S, O, and C were observed. The peaks of C and O came from the reference sample and adsorbed oxygen (Zhou et al. 2014). The atomic ratio of [S] : [In] was estimated to be 1.43 from the survey spectrum confirming In_2S_3. The result was little smaller than the theoretical value of 1.5, which indicated the existence of sulfur vacancies or oxidation on the as-synthesized In_2S_3 sample surfaces (Tian et al. 2013). Fig. 4(c-d) showed In 3d and S 2p high-resolution region spectra, respectively. The peaks at the binding energy value of 444.8 and 452.4 eV were related to In $3d_{5/2}$

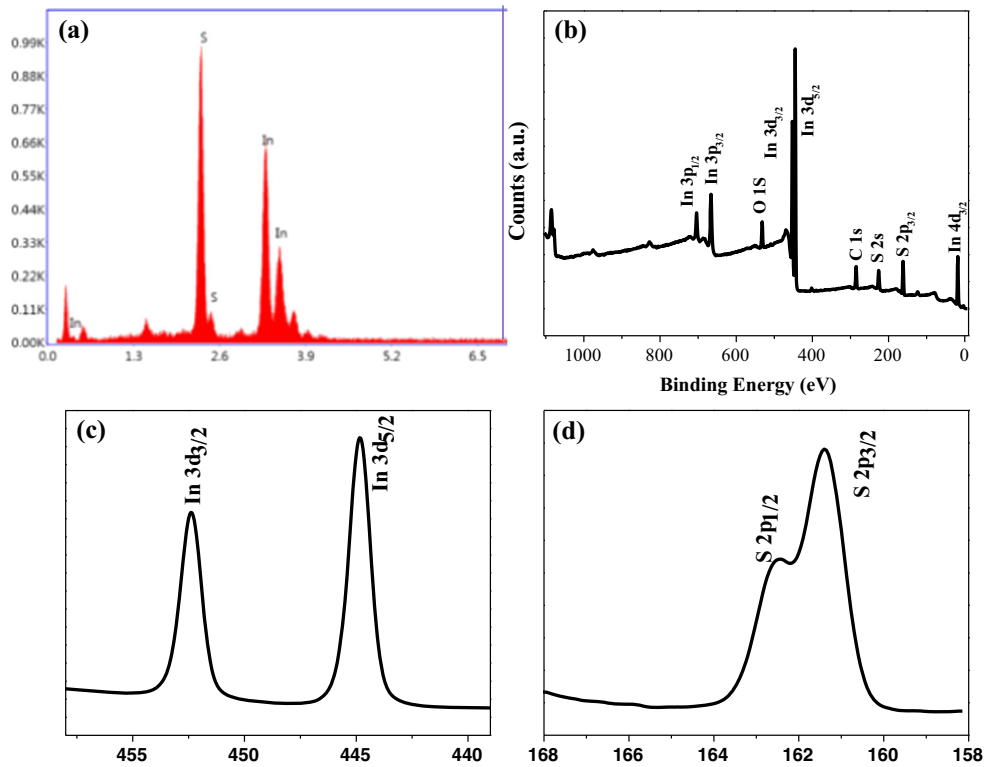

Fig. 4 XPS region spectra of the hierarchical flower-like β-In_2S_3: (a) EDX spectrum; (b) XPS survey spectrum; (c) In 3d ; (d) S 2p.

and In $3d_{3/2}$, while the peaks at 161.4 and 162.4 eV could be attributed to S $2p_{3/2}$ and S $2p_{1/2}$ transitions (Nayak et al. 2014; Gao et al. 2015b), respectively. The observed binding energy values of In 3d and S 2p agreed well with the reported data for In_2S_3 (Chai et al. 2012). To further study the O state on the surface of the In_2S_3, the high resolution O 1s XPS spectrum was analyzed and exhibited in Fig. 5. As shown in Fig. 5, the O 1s peak of In_2S_3 could be deconvoluted into three peaks. The peak located at around 530.8 eV, which was indexed to the oxygen from the crystal lattice (O^{2-}). The other two peaks at 531.6 eV and 532.8 eV were referred to surface hydroxyl oxygen of adsorbed water and adsorbed oxygen from the ambient atmosphere, respectively (Du et al. 2009).

Porous structure determination by N_2 adsorption / desorption

The specific surface area and porosity of the flower-like β-In_2S_3 hierarchical structures assembled by 2D thin nanosheets were further investigated by the nitrogen adsorption-desorption method. Fig. 6a showed the typical sorption isotherms and the corresponding pore size distribution (inset of Fig. 6a) of the flower-like β-In_2S_3. The type-IV isotherm with a hysteresis loop was obtained which could be identified as characteristic of mesoporous materials. These mesopores arose from the spaces among the nanosheets, consistent with the result of the HRTEM measurement. Accordingly, the pore size distribution

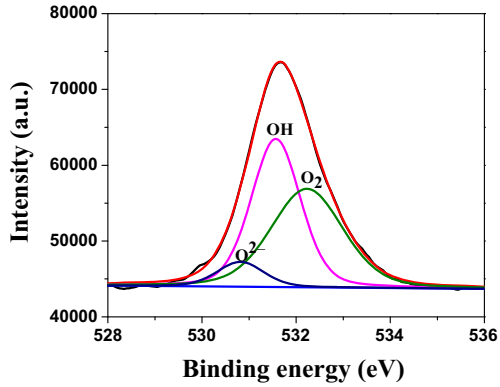

Fig. 5 O 1s region XPS spectra of the In_2S_3 sample

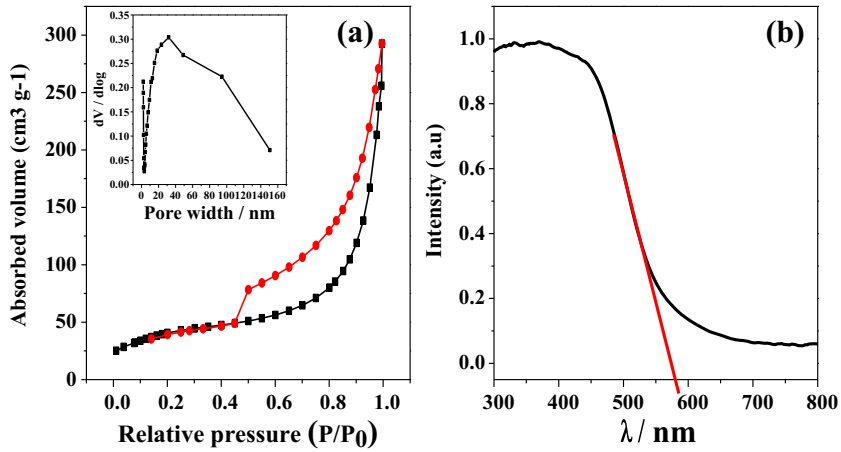

Fig. 6 As-prepared hierarchical flower-like β-In_2S_3: (a) N_2 adsorption/desorption isotherm curves (inset: BJH pore size distribution plot); (b) UV-vis DRS spectrum.

curve depicted a wide range of pore size distribution from 2 to 150 nm with a unimodal shape at 32 nm. The BET surface area of as-prepared the hierarchical flower-like β-In_2S_3 was calculated to be 134.1 m^2 g^{-1}. The as-prepared hierarchical flower-like β-In_2S_3 showed the higher surface area among various previously reported In_2S_3 nanomaterials (Table 1). The large surface area would facilitate the surface adsorption of reactants and promote interfacial charge transfer (Zhou et al. 2013), and improve the photocatalytic properties.

DRS property

The optical absorption properties of a semiconductor were relevant to the electronic features, and recognized as a key factor in determining it photocatalytic activity. Fig. 6b showed the UV-vis diffuse reflectance spectra (DRS) of the hierarchical flower-like β-In_2S_3. The band gap (E_g) of In_2S_3 was reported to vary between 2.0 and 2.2 eV, which corresponded to 620-550 nm (Rengaraj et al. 2011). The absorption edge about 580 nm was evidently seen, demonstrating that the band gap of the

Table 1 the summary of reported BET surface area of various In_2S_3 materials

Catalyst	BET surface area/m^2 g^{-1}	Reference
3D fowerlike In_2S_3 microspheres	72.9	(Wei et al. 2014)
Hierarchical-like β-In_2S_3 hollow microspheres	108	(Rengaraj et al. 2011)
In_2S_3 nanoparticles	31.1	(Liu et al. 2011)
In_2S_3 nanotubes	72.0	(Liu et al. 2011)
3D hierarchical porous In_2S_3 microspheres	90.09	(Wu et al. 2015)
Nanocrystal In_2S_3	130.7	(He et al. 2009)
In_2S_3 microspheres	103.05	(Nayak et al. 2014)
In_2S_3 nanoparticles	110	(Yang et al. 2013)
In_2S_3 nanoparticles	70.74	(Gao et al. 2015b)
Porous 3D flower-like β-In_2S_3 structures	78	(Chen et al. 2008)
Flower-like β-In_2S_3	117	(Xue et al. 2010)
Walnut-like In_2S_3 microspheres	18.8	(Chai et al. 2012)
Mesoporous β-In_2S_3 microspheres	15.2	(Li and Liu 2011a)
Mesoporous β-In_2S_3@C microspheres	31.3	(Li and Liu 2011)
In_2S_3 microspheres	158.2	(Chen et al. 2016)
Flower-like In_2S_3 hierarchical structures assembled by 2D nanosheets	134.08	Present work

product was about 2.14 eV. Moreover, the hierarchical flower-like β-In_2S_3 had strong absorption ranging from the visible to UV region, suggesting great effect of light absorption.

Adsorption performance

To investigate the surface charge of as-prepared sample, zeta potential measurement was carried out. The hierarchical flower-like β-In_2S_3 had a low overall charge with a zeta potential of about -24.2 mV, which could be due to the adsorption of -OH on the In_2S_3 surface in aqueous solution. This could promote efficient adsorption through providing adsorption sites for interaction with the cationic groups of MB.

Adsorption kinetics studies were explored at different time interval of MB (35 mg L^{-1}) and adsorbent (10 mg) interaction. Fig. 7a showed adsorption kinetic of MB on In_2S_3 at 298 K. Both pseudo-first-order and pseudo-second-order kinetics were tested using the experimental data of MB removal from aqueous solutions. The pseudo-first-order rate equation is given by the following equation (Mittal et al. 2009):

$$\ln(Q_e - Q_t) = \ln(Q_{e1}) - k_1 t \quad (1)$$

where Q_e and Q_t are the amounts of dye adsorbed at equilibrium (mg g^{-1}) and at contact time t (min), respectively. Q_{e1} and k_1 show the theoretical equilibrium adsorption and rate constant of pseudo-first-order kinetic, respectively. The values k_1 and Q_{e1} could be determined from the slope and the intercept of the plot of $\ln(Q_e - Q_t)$ against t and presented in Fig. 7b. The rate of pseudo-second-order model depend on the amount and the quantity of dye adsorbed on the surface of adsorbent (Gucek et al.

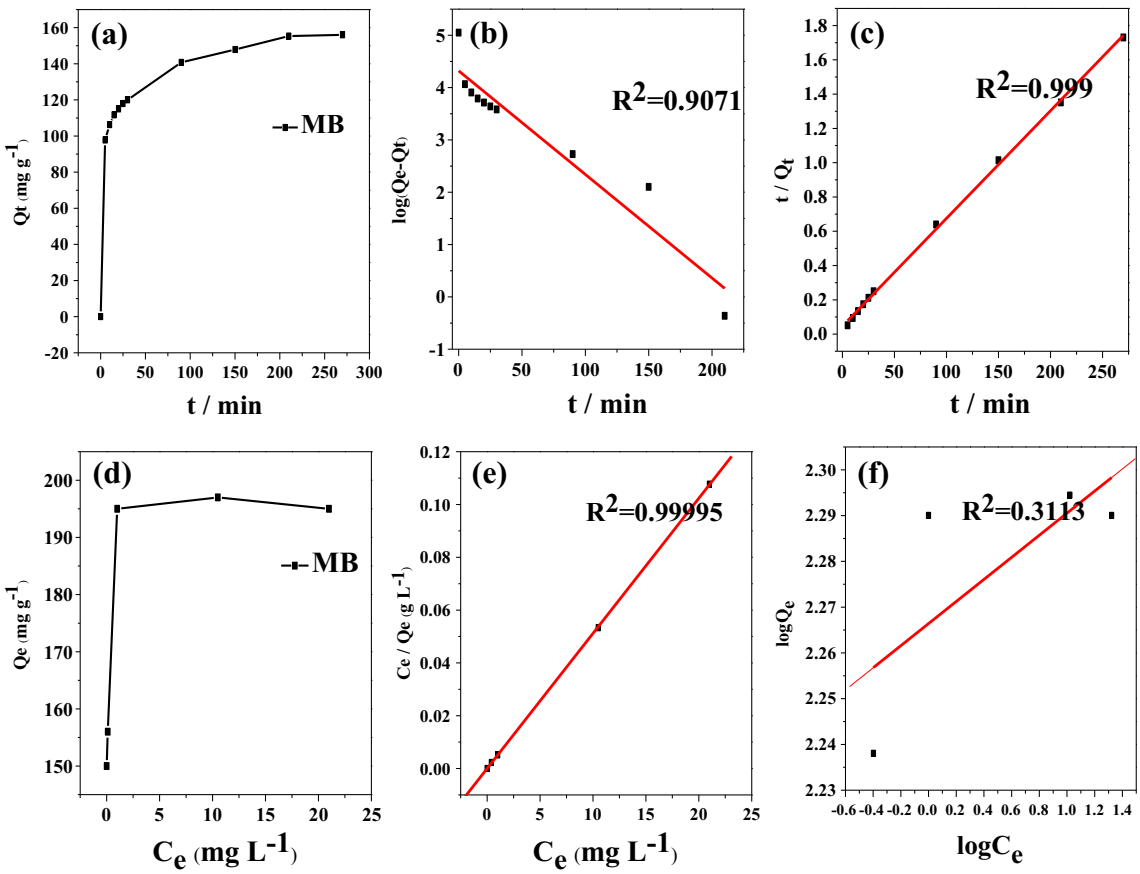

Fig. 7 (a) Adsorption kinetic (T = 298 K; C_0 = 35 mg L^{-1}; amount of adsorbent = 10 mg; volume of solution = 50 mL); (b) Pseudo-first-order kinetics; (c) Pseudo-second-order kinetics; (d) Adsorption isotherm (T=298 K; adsorbent dose =10 mg; dye concentration = 30-60 mg L^{-1}; solution volume = 50 mL); (e) Langmuir isotherm; (f) Freundlich isotherm.

2005). The pseudo-second-order rate can be expressed as follows (Gupta et al. 2010):

$$t/Q_t = 1/k_2(Q_{e2})^2 + t/Q_{e2} \quad (2)$$

where k_2 (g mg^{-1} min^{-1}) is the pseudo-second-order rate constant, and Q_{e2} is the theoretical adsorbed dye (mg g^{-1}). In this case, the slope and the intercept of the plot of t/Q_e vs t gave k_2 and Q_{e2} values as presented in Fig. 7c. As it could be seen from Table 2, the high R^2 value suggested that the pseudo-second-order kinetic model was more suitable than pseudo-first-order kinetic model for the MB removal. Moreover, the Q_{e2} value for the second-order kinetic was close to the experiment ($Q_{e,exp}$). This behavior could be explained with the existence of chemisorptions (Saha et al. 2012), which was in accordance with literature result (Madaeni et al. 2011).

To further investigate the adsorption mechanism, Langmuir and Freundlich models were used to describe the equilibrium of adsorption. Fig. 7d showed adsorption isotherm of MB on In_2S_3 at 298 K. It is known that the Langmuir model predicts the formation of a monolayer of the adsorbate on the adsorbent surface, while the Freundlich isotherm is an empirical equation for the description of equilibrium on heterogeneous surfaces. The isotherm linear forms of Langmuir and Freundlich are expressed by Eqs. (3) and (4), respectively:

$$C_e/Q_e = C_e/Q_m + 1/(K_L Q_m) \quad (3)$$

$$\log Q_e = \log K_F + \frac{1}{n}\log C_e \quad (4)$$

Where Q_e is the amounts of dye adsorbed at equilibrium (mg g^{-1}), C_e is the final concentration in solution of dye adsorbed at equilibrium (mg L^{-1}), K_L is the Langmuir constant (L mg^{-1}), depending upon the adsorption energy, and Q_m is the maximum adsorption capacity (mg g^{-1}). K_F (mg g^{-1}) is the adsorption capacity of the adsorbent and n (L mg^{-1}) is the Freundlich constant. C_e/Q_e against C_e and $\log Q_e$ against $\log C_e$ were plotted shown in Fig. 7e and f. And the data were analyzed by linear regression, the values of Q_m and K_L, n and K_F calculated from the slope and intercept, respectively.

As it can be seen from Table 3, the Langmuir model showed the best fit (R^2 = 0.9999) with a saturated coverage of 195.3 mg g^{-1}, which was close to the experimental data (195.5 mg g^{-1}). Therefore, monolayer adsorption was concluded and the adsorption sites were homogeneous.

Photodecolorization performance

To evaluate the photoactivity of catalysts, methyl orange (MO), a very stable azo dye, was used as a model pollutant (An et al. 2013). UV-vis absorption measurement was a very simple and direct method to study small molecule substances with subtle changes in molecule structure. Without In_2S_3, almost no color removed of the MO after 4 h of irradiation (Fig. 8a). Before the irradiation, minimum decrease in MO concentration was observed after stirring the mixture of MO and In_2S_3 for 30 min in the dark condition (Fig. 8b). As could be observed from these spectra, the maximum absorption located at 465 nm and 270 nm. The peak at 465 nm was originated from an extended chromophore— azo linkage and the peak at 270 nm was associated with benzene ring in the molecule, respectively (Zhang et al. 2006). After irradiation, the intensity of the two peaks disappeared after 15 min of irradiation, indicating the destruction of its chromophoric structure (Fig. 8c). The photocatalytic decolorization kinetics of MO were shown in Fig. 8d, although the ratio of C/C_0 decreased with the illumination time was quickly, the ratio of TOC/TOC_0 decreased with the illumination time was slowly. These results indicated that MO was successfully decolorized to a colorless state by In_2S_3, but the MO molecules could not be fully photomineralized. As reported in several literatures, the intermediates were stable in the system which required a longer time for further oxidation (Nur Farhana et al. 2012; Yu et al. 2016). The MS

Table 2 Summary of the kinetic constants obtained from linear regression of the two models

Pseudo-first-order			Pseudo-second-order		
k_1 (min^{-1})	Q_{e1} (mg g^{-1})	R^2	k_2 (g mg^{-1}min^{-1})	Q_{e2} (mg g^{-1})	R^2
0.01	75.3	0.907	0.0008	159.2	0.999

Table 3 Correlation coefficients and isotherm rate constants for Langmuir and Freundlich models

Model	Parameters	Values
Langmuir	Q_m(mg g^{-1})	195.3
	K_L(L mg^{-1})	0.0031
	R^2	0.9999
Freundlich	K_F (mg g^{-1})	184
	n	41.49
	R^2	0.3113

analysis was performed for MO decolorization, and the formation of intermediates during the decolorization process was identified by this technique. The sample before the MO decolorization showed one big peak at m/z 304. In contrast, the sample after 15 min of decolorization showed one main m/z peak at 172, corresponding to 4-aminosulfonic acid (Han et al. 2016). The results suggested that decolorization proceeds through the cleavage of azo group —N=N— connecting the two aromatic rings to amines, which agreed with literature results (Parshetti et al. 2010). Clearly, the decoloration of MO was attributed to the photocatalytic decolorization instead of adsorption.

We further studied the durability and the recyclability of the hierarchical flower-like β-In_2S_3 for the decolorization of MO. The decolorization efficiency was maintained at 98.8% after the sixteenth cycle (Fig. 9c), indicating a negligible change in decolorization performance and high stability of the catalyst. After the sixteenth cycle of the decolorization experiment, the catalyst powder was collected by centrifugation and dried at 60 °C for 4 h. The phase of used catalyst was remained unchanged (Fig. 9d).

Different pathways were reported for the visble-light-driven photodecolorization of MO, which could be classified according to the active species (An et al. 2013; Gao et al. 2015a). Trapping experiments were conducted to determine the main active species during the photodecolorization process. Benzoquinone (BQ), isopropyl alcohol (IPA), EDTA-2Na, and

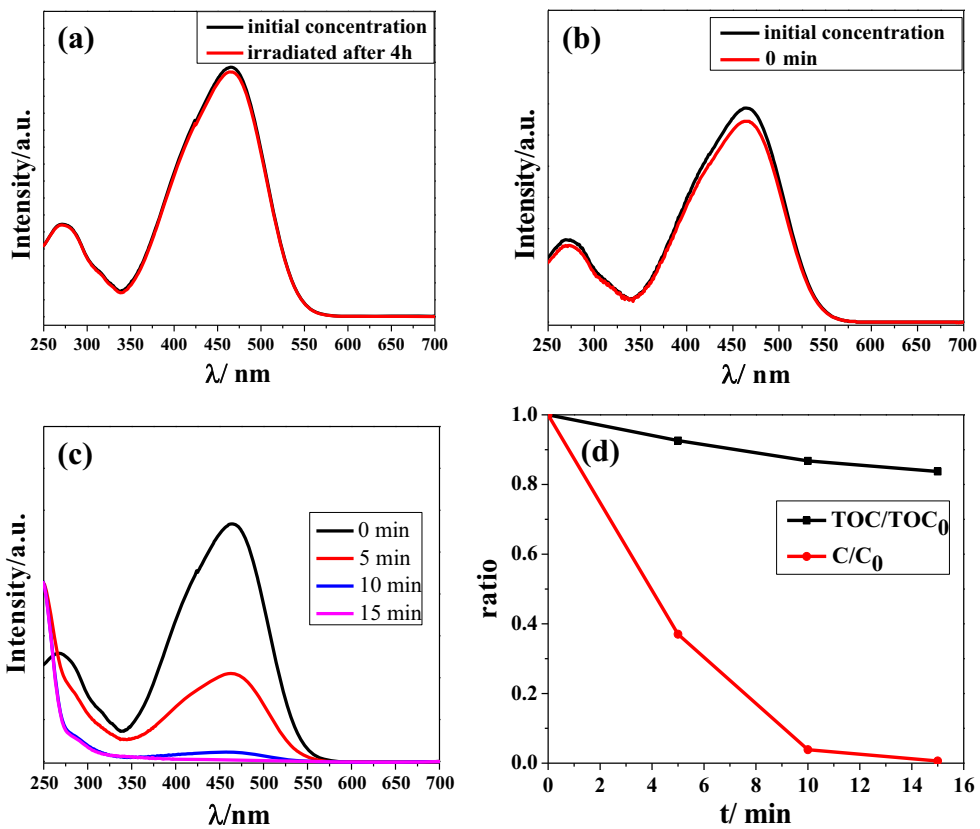

Fig. 8 Time-dependent UV-vis absorption spectra of MO: (a) Without β-In_2S_3, (b) With β-In_2S_3 under dark condition, and (c) With β-In_2S_3 under visible light; (d) Photocatalytic degradation kinetics of MO.

$K_2Cr_2O_7$ were used as scavengers of superoxide radical ($\cdot O_2^-$), hydroxyl radical ($\cdot OH$), h^+ and e^{-1} (Song et al. 2016). As shown in Fig. 9a, the decolorization of MO molecules was attributed to the predominant action of oxidation action of the generated $\cdot O_2^-$ radicals and subordinate e^{-1} reduction process. Hydroxyl radical was confirmed to be insignificant for the decolorization of MO (Li et al. 2011). The CB and VB potentials (E_{CB} and E_{VB}) of the β-In_2S_3 can be calculated by the empirical equations of $E_{CB} = \chi - E_e - 0.5E_g$ and $E_{VB} = E_{CB} + E_g$, where $E_g = 2.14$ eV, χ is the electronegativity of the In_2S_3 (4.69 eV), E_e is the energy of free electrons on the hydrogen scale (about 4.5 eV) (Chen et al. 2016). Therefore,the value of E_{CB} and E_{VB} are -0.88 and 1.06 eV for the β-In_2S_3. The valance band of In_2S_3 was more negative than E ($\cdot OH/OH^-$) (2.38 V vs. NHE) and E ($\cdot OH/H_2O$) (2.27 V vs. NHE), hence the photoinduced holes could not oxidize OH^- and H_2O to produce $\cdot OH$. Instead, they could oxidize the dye macromolecules into directly micromolecules and final products (Cheng et al. 2010). While the conduction band of In_2S_3 was more negative than E ($O_2/\cdot O_2^-$) and the photogenerated electrons of the In_2S_3 sample were enough to generate $\cdot O_2^-$ under visible irradiation. The schematic demonstration of the excitation and charge

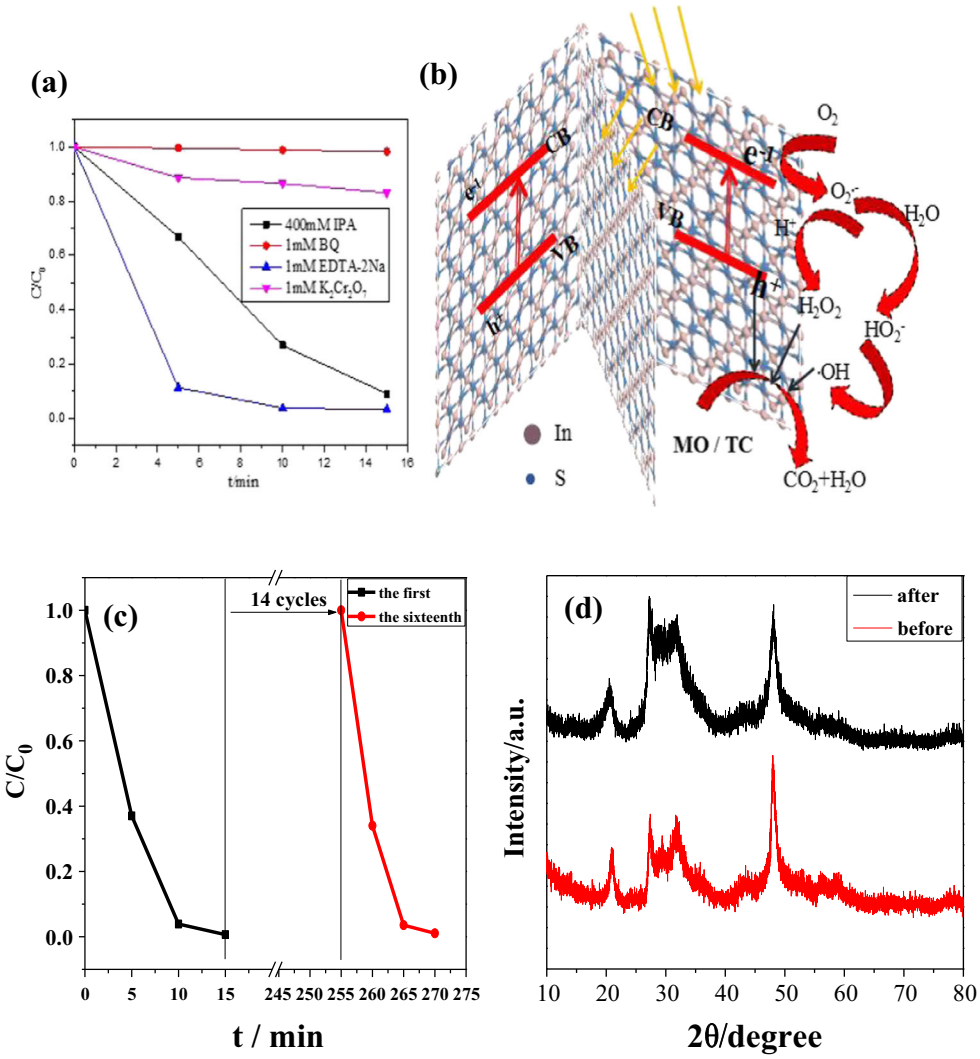

Fig. 9 (a) In_2S_3 catalyst activity of capture agent; (b) Proposed mechanisms of photocatalytic reaction in In_2S_3 system, the nets structure is In_2S_3 nanosheet; (c) Photocatalytic decolorization curves of MO under visible light irradiation the first and the sixteenth cycles; (d) XRD patterns of as-prepared In_2S_3 before and after 16 cycles.

transfer processes of the hierarchical flower-like β-In_2S_3 under visible light irradiation was shown in Fig. 9b. The proposed mechanism for the photocatalytic decomposition of MO by the flower-like β-In_2S_3 assembled by 2D thin nanosheets can be described as follows:

$$In_2S_3 + h\nu \rightarrow In_2S_3\left(e^{-1} + h^{+}\right)$$

$$O_2 + 2H^{+} + 2e^{-1} \rightarrow H_2O_2 \qquad E^{\theta} = 0.6824\ V$$

$$O_2 + e^{-1} \rightarrow O_2^{\cdot -} \qquad E^{\theta} = -0.563\ V$$

$$O_2^{\cdot -} + H_2O + e^{-1} \rightarrow HO_2^{-} + OH^{-} \qquad E^{\theta} = 0.413\ V$$

$$HO_2^{-} + H_2O + e^{-1} \rightarrow {}^{\cdot}OH + 2OH^{-} \qquad E^{\theta} = 0.878\ V$$

$$h^{+}/H_2O_2/{}^{\cdot}OH + MO \rightarrow \text{degraded or mineralized products}$$

The hierarchical flower-like β-In_2S_3 assembled by 2D nanosheets was also a highly effective photocatalyst for antibiotics removal under visible light irradiation. The catalytic degradation of antibiotics was of great importance because they posed serious threats to the ecosystem and human health even at small concentrations in water system. As shown in Fig. 10, TC could hardly be decolored without any photocatalyst (Fig. 10a), while the flower-like β-In_2S_3 showed high activity with decolorization rate of 90.1 % after visible light irradiation for 60 min. The decolorization speed of TC was much faster than previously reported systems (Wang et al. 2016; Ai et al. 2015).

The as-synthesized hierarchical flower-like β-In_2S_3 occurred a rapid decolorization reaction that may be due to the following several reasons for synergism. The first reason was attributed to its cubic phase crystal structure. Naik et al. (2008) reported that the cubic In_2S_3 showed higher photoactivity for hydrogen production than of tetragonal β-In_2S_3. Dai *et al*. (2010) proposed that cubic In_2S_3 had not the three-dimensional defect structure resulted from the ordering of indium vacancies, hence the charges transportation efficiency of the pathway would not be depressed. Meanwhile, sulfur vacancies in the as-synthesized In_2S_3 surfaces might exhibit electron affinity and could act as electron traps which promoting the separation of photogenerated charge carriers (Gao et al. 2015b). Moreover, the sample contained oxygen from the crystal lattice was more propitious to form the defect band (Chen et al. 2016). Second, not only the high surface area but also the wide range of pore size distribution of the flower-like In_2S_3 led to greater contact possibility with pollutants and provided more active catalytic sites (Dai et al. 2010; Li et al. 2014). Third, the smaller size of the flower-like β-In_2S_3 hierarchical structures than other flower-like β-In_2S_3 microspheres (Wei et al. 2014; Liu et al. 2011) (> 2 μm) could effectively shorten the diffusion distance for carriers (Maeda 2011; Mi et al. 2015). Finally, the photoexcited carriers separated and migrated to the surface with less recombination as a result of the ultrathin sheet (Mi et al. 2015).

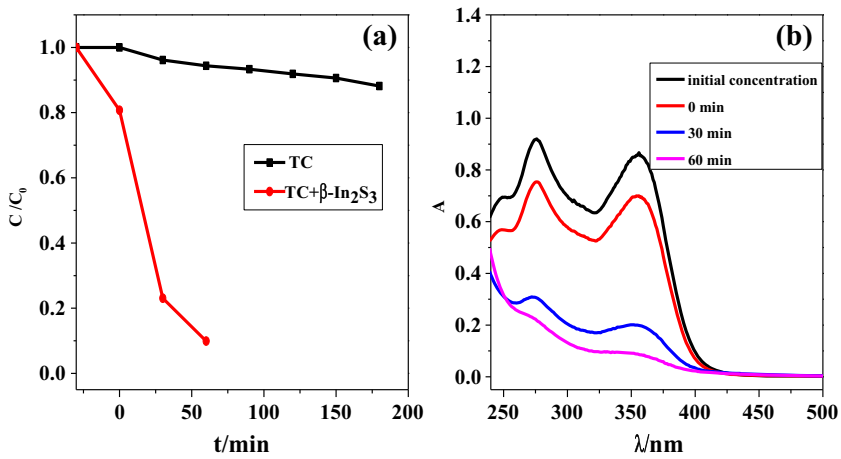

Fig. 10 (a) Time-dependent UV-vis absorption spectra; (b) Photocatalytic decolorization curves of TC under visible light in the presence of the hierarchical flower-like β-In_2S_3.

Conclusion

In summary, a simple and facile method was developed to transform single-source precursor In-DDTC into flower-like In_2S_3 hierarchical structures assembled by 2D thin nanosheets. The flower-like In_2S_3 material showed high adsorption property for MB and great decolorization property for MO and TC under the visible light irradiation. The decreased speed of the TOC was slower than the MO concentration. Several factors including its unique structures were proposed to be responsible for the great properties. This facile and promising synthetic strategy could be extended to prepare a wide variety of functional materials for potential applications including photocatalytic reactions, hydrogen production, solar cells and lithium-ion batteries.

Acknowledgements This work was supported by the National Natural Science Foundation of China (grant Nos. 21471001, 21275006 and 21575001), Key Project of Anhui Provincial Education Department (KJ2013A029) and Natural Science Foundation of Anhui Province (1508085MB32).

Compliance with Ethical Standards

Conflict of interest The authors declare that they have no conflict of interest.

Human and Animal Rights All procedures performed in studies involving human participants were in accordance with the ethical standards.This article does not contain any study with animals performed by any of the authors. Informed consent was obtained from all individual participants included in the study.

References

Abdelhady AL, Ramasamy K, Maik MA, O'Brien P (2013) Very narrow In_2S_3 nanorods and nanowires from a single source precursor. Mater Lett 99:138–141

Ai CL, Zhou DD, Wang Q, Shao XW, Lei YJ (2015) Optimization of operating parameters for photocatalytic degradation of tetracycline using In_2S_3 under natural solar radiation. Solar Energy 113:34–42

An XQ, Yu JC, Wang F, Li CH, Li YC (2013) One-pot synthesis of In_2S_3 nanosheets/graphene composites with enhanced visible-light photocatalytic activity. Appl Catal B- Environ 129:80–88

Chai B, Zeng P, Zhang XH, Mao J, Zan L, Peng TY (2012) Walnut-like In_2S_3 microspheres: ionic liquid-assisted solvothermal synthesis, characterization and formation mechanism. Nanoscale 4:2372–2377

Chen LY, Zhang ZD, Wang WZ (2008) Self-assembled porous 3D flowerlike β-In_2S_3 structures: synthesis, characterization, and optical properties. J Phys Chem C 112:4117–4123

Chen J, Liu WX, Gao WW (2016) Tuning photocatalytic activity of In_2S_3 broad band spectrum photocatalyst based on morphology. Appl Surf Sci 368:288–297

Cheng HF, Huang BB, Dai Y, Qin XY, Zhang XY (2010) One-step synthesis of the nanostructured AgI/BiOI composites with highly enhanced visible-light photocatalytic performances. Langmuir 26:6618–6624

Dai XJ, Luo YS, Zhang WD, Fu SY (2010) Facile hydrothermal synthesis and photocatalytic activity of bismuth tungstate hierarchical hollow spheres with an ultrahigh surface area. Dalton Trans 39:3426–3432

Du WM, Zhu J, Li SX, Qian XF (2008) Ultrathin beta-In_2S_3 nanobelts: Shape-controlled synthesis and optical and photocatalytic properties. Cryst Growth Des 8:2130–2136

Du J, Huang L, Chen Z (2009) A Controlled method to synthesize hybrid In_2O_3/Ag nanochains and nanoparticles: surface-enhanced raman scattering. J Phys Chem C 113:9998–10004

Gao T, Chen Z, Niu F, Zhou DT, Huang QL, Zhu YX, Qin LS, Sun XG, Huang YX (2015a) Shape-controlled preparation of bismuth ferrite by hydrothermal method and their visible-light degradation properties. J Alloys Compd 648:564–570

Gao WW, Liu WX, Leng YH, Wang XW, Wang XQ, Hu B, Yu DH, Sang YH, Liu H (2015b) In_2S_3 nanomaterial as a broad-band spectrum photocatalyst to display significant activity. Appl Catal B-Environ 176-177:83–90

Gorai S, Chaudhuri S (2005) Sonochemical synthesis and characterization of cage-like beta-indium sulphide powder. Mater Chem Phys 89:332–335

Gucek A, Sener S, Bilgen S, Mazmanci ML (2005) Adsorption and kinetic studies of cationic and anionic dyes on pyrophyllite from aqueous solutions. J Colloid Interf Sci 286:53–60

Guo YQ, Xu K, Wu CZ, Zhao JY, Xie Y (2015) Surface chemical-modification for engineering the intrinsic physical properties of inorganic two-dimensional nanomaterials. Chem Soc Rev 44:637–646

Gupta VK, Rastogi A, Nayak A (2010) Biosorption of nickel onto treated alga (Oedogonium hatei): Application of isotherm and kinetic models. J Colloid Interf Sci 342:533–539

Han J, Zeng HY, Xu S, Chen CR, Liu XJ (2016) Catalytic properties of CuMgAlO catalyst and degradation mechanism in CWPO of methyl orange. Appl Catal A- Gen 527:72–80

He YH, Li DZ, Xiao GC, Chen W, Chen YB, Sun M, Huang HJ, Fu XZ (2009) A New Application of nanocrystal In_2S_3 in efficient degradation of organic pollutants under visible light irradiation. J Phys Chem C 113:5254–5262

Lee SS, Yoon SH, Seo KW, Shin IW (2005) Preparation of In_2S_3 thin films by MOCVD using single source precursors: Tris (N, N-ethylbutyldithiocarbamato) indium(III) and tris(2-ethylpiperidinedithiocarbamato)indium(III) Bull. Korean Chem Soc 26:1453–1456

Li G, Liu HJ (2011) Improved electrode performance of mesoporous β-In_2S_3 microspheres for lithium ion batteries using carbon coated microspheres. J Mater Chem 21:18398–18402

Li YY, Wang JS, Yao HC, Dang LY, Li ZJ (2011) Efficient decomposition of organic compounds and reaction mechanism with BiOI photocatalyst under visible light irradiation. J Mol Catal A-Chem 334:116–122

Li YG, Zhu LP, Guo YM, Song H, Lou ZR, Ye ZZ (2014) A new type of hybrid nanostructure: complete photo-generated carrier separation and ultrahigh photocatalytic activity. J Mater Chem A 2:14245–14250

Li GW, Su R, Rao JC, Wu JQ, Rudolf P, Blake GR, Groot RA, Besenbacher F, Palstra TTM (2016) Band gap narrowing of SnS_2 superstructures with improved hydrogen production. J Mater Chem A 4:209–216

Liu GD, Jiao XL, Qin ZH, Chen DR (2011) Solvothermal preparation and visible photocatalytic activity of polycrystalline β-In_2S_3 nanotubes. CrystEngComm 13:182–187

Liu CB, Meng DS, Li Y, Wang LL, Liu YT, Luo SL (2015) Hierarchical architectures of ZnS-In_2S_3 solid solution onto TiO_2 nanofibers with high visible-light photocatalytic activity. J Alloys Compd 624:44–52

Luo J, Jiang H, Huang J (2013) Effect of sheet morphology on the scalability of graphene-based ultracapacitors. ACS Nano 7: 1464–1471

Madaeni SS, Jamali Z, Islami N (2011) Highly efficient and selective transport of methylene blue through a bulk liquid membrane containing Cyanex 301 as carrier. Sep Purif Technol 81:116–123

Maeda K (2011) Photocatalytic water splitting using semiconductor particles: History and recent developments. J Photoch Photobio C 12:237–268

Meng NN, Zhou YF, Nie WY, Chen PP (2016) Synthesis of CdS-decorated RGO nanocomposites by reflux condensation method and its improved photocatalytic activity. J Nanopar Res 18:241

Mi Y, Wen LY, Wang ZJ, Cao DW, Fang YG, Lei Y (2015) Building of anti-restack 3D BiOCl hierarchitecture by ultrathin nanosheets towards enhanced photocatalytic activity. Appl Catal B- Environ 176-177:331–337

Mittal A, Mittal J, Malviya A, Gupta VK (2009) Adsorptive removal of hazardous anionic dye "Congo red" from wastewater using waste materials and recovery by desorption. J Colloid Interf Sci 340:16–26

Naik SD, Jagadale TC, Apte SK, Sonawane RS, Kulkarni MV, Patil SI, Ogale SB, Kale BB (2008) Rapid phase-controlled microwave synthesis of nanostructured hierarchical tetragonal and cubic β-In_2S_3 dandelion flowers. Chem Phys Lett 452:301–305

Nayak AK, Lee S, Sohn Y, Pradhan D (2014) Synthesis of In_2S_3 micro-spheres using a templatefree and surfactant-less hydrothermal process and their visible light photocatalysis. CrystEngComm 16:8064–8072

Nur Farhana J, Aishah AJ, Sugeng T, Muhd Nazlan MM, Norzahir S, Mohammad Azrul HS, Hanak A (2012) Photodecolorization of methyl orange over -Fe_2O_3- supported HY catalysts: The effects of catalyst preparation and dealumination. Chem Eng J 191:112–122

Park KH, Jang K, Son SU (2006) Synthesis, optical properties, and self-assembly of ultrathin hexagonal In_2S_3 nanoplates. Angew Chem Int Ed 45:4608–4612

Parshetti GK, Telke AA, Kalyani DC, Govindwar SP (2010) Decolorization and detoxification of sulfonated azo dye methyl orange by *Kocuria rosea* MTCC 1532. J Hazard Mater 176:503–509

Patra CR, Patra S, Gabashvili A, Mastai Y, Gedanken Y, Palchik A, Slifkin MA (2006) A microwave route for the synthesis of nanoflakes and dendrites-type, beta-In_2S_3 and their characterization. J Nanosci Nanotechnol 6:845–851

Rengaraj S, Venkataraj S, Tai CW, Kim Y, Repo E, Sillanpaa M (2011) Self-assembled mesoporous hierarchical-like In_2S_3 hollow microsperes composed of nanofibers and nanosheets and their photocatalytic activity. Langmuir 27:5534–5541

Saha PD, Chakraborty S, Chowdhury S (2012) Batch and continuous (fixed-bed column) biosorption of crystal violet by *Artocarpus heterophyllus* (jackfruit) leaf powder. Colloids Surfaces B 92:262–270

Song JL, Wang BY, Guo XJ, Wang RF, Dong ZP (2016) Hierarchical nanostructured 3D flowerlike BiOX particles with excellent visible-light photocatalytic activity. J Nanopar Res 18:245

Sun MH, Huang SZ, Chen LH, Li Y, Yang XY, Yuan ZY, Su BL (2016) Applications of hierarchically structured porous materials from energy storage and conversion, catalysis, photocatalysis, adsorption, separation, and sensing to biomedicine. Chem Soc Rev 45:3479–3563

Tian J, Sang Y, Yu G, Jiang H, Mu X, Liu H (2013) A Bi_2WO_6-Based hybrid photocatalyst with broad spectrum photocatalytic properties under UV, visible, and near-infrared irradiation. Adv Mater 25:5075–5080

Wang XX, Zhao CH, Liu R, Shen Q (2014) Hydrothermal synthesis and structural properties of hierarchical flower-like SnO_2 nanostructures for lithium ion batteries. J Nanopar Res 16:2570

Wang L, Liu JJ, Zhang LL, Dai BS, Xu M, Ji MW, Zhao XS, Cao CB, Zhang JT, Zhu HS (2015) Rigid three-dimensional Ni_3S_4 nanosheet frames: controlled synthesis and their enhanced electrochemical performance. RSC Adv 5:8422–8426

Wang H, Yuan XZ, Wu Y, Zeng GM, Dong HR, Chen XH, Leng LJ, Wu ZB, Peng LJ (2016) In situ synthesis of In_2S_3@MIL-125(Ti) core-shell microparticle for the removal of tetracycline from wastewater by integrated adsorption and visible-light-driven photocatalysis. Appl Catal B- Environ 186:19–29

Wei CY, Guo W, Yang JQ, Fan HM, Zhang J, Zheng WJ (2014) Facile solvothermal synthesis of 3D flowerlike β-In_2S_3 microspheres and their photocatalytic activity performance. RSC Adv 4:50456–50463

Wu X, Fu Y, Liu Y, Xu Y, Liu C, Zhang B (2012) Synthesis of hollow Cd_xZn1-xSe nanoframes through the selective cation exchange of inorganic- organic hybrid ZnSe-amine nanoflakes with cadmium ions. Angew Chem Int Ed 51: 3211–3215

Wu DX, Duan JF, Zhang CY, Guo K, Zhu HT (2013a) Sacrificial Template Synthesis and Photothermal Conversion Enhancements of Hierarchical and Hollow $CuInS_2$ Microspheres. J Phys Chem C 117:9121–9128

Wu HB, Pang H, Lou XW (2013b) Facile synthesis of mesoporous $Ni_{0.3}Co_{2.7}O_4$ hierarchical structures for high-performance supercapacitors. Energy Environ Sci 6:3619–3626

Wu R, Xu Y, Xu R, Huang Y, Zhang B (2015) Ultrathin-nanosheet-based 3D hierarchical porous In_2S_3 microspheres: chemical transformation synthesis, characterization, and enhanced photocatalytic and photoelectrochemical property. J Mater Chem A 3:1930–1934

Xia JX, Ji MX, Di J, Wang B, Yin S, Zhang Q, He MQ, Li HM (2016) Construction of ultrathin $C_3N_4/Bi_4O_5I_2$ layered nanojunctions via ionic liquid with enhanced photocatalytic

performance and mechanism insight. Appl Catal B-Environ 191:235–245

Xiao ZL, Han CY, Kwok WK, Wang HH, Welp U (2004) Tuning the Architecture of Mesostructures by Electrodeposition. J Am Chem Soc 126:2316–2317

Xue KY, Chen DR, Jiao XL (2010) Fabrication of crystalline mesoporous metal oxides and sulfides. Inorg Chem 49: 1191–1197

Yang MQ, Weng B, Xu YJ (2013) Improving the Visible Light Photoactivity of In_2S_3-Graphene Nanocomposite via a Simple Surface Charge Modification Approach. Langmuir 29:10549–10558

Yu ZY, Qiu RY, Li HR, Wang ZY, Ma XH, Dong CN (2016) Preparation and photocatalytic activity of SnO_2. Mater Lett 170:25–30

Zhang XD, Xie Y (2013) Recent advances in free-standing two-dimensional crystals with atomic thickness: design, assembly and transfer strategies. Chem Soc Rev 42:8187–8199

Zhang YC, Wang GY, Hu XY, Shi QF, Qiao T, Yang Y (2005) Phase-controlled synthesis of ZnS nanocrystallites by mild solvothermal decomposition of an air-stable single-source molecular precursor. J Cryst Growth 284:554–560

Zhang H, Duan LJ, Zhang DB (2006) Decolorization of methyl orange by ozonation in combination with ultrasonic irradiation. J Hazard Mater B 138:53–59

Zhang Y, Sun WP, Rui XH, Li B, Tan HT, Guo G, Si M, Zong Y, Yan QY (2015) One-Pot Synthesis of Tunable Crystalline Ni_3S_4@Amorphous MoS_2 Core/Shell Nanospheres for High-Performance Supercapacitors. Small 11:3694–3702

Zhou M, Lou XW, Xie Y (2013) Two-dimensional nanosheets for photoelectrochemical water splitting: Possibilities and opportunities. Nano Today 8:598–618

Zhou J, Tian GH, Chen YC, Shi YH, Tian CG, Pan K, Fu HG (2014) Growth rate controlled synthesis of hierarchical Bi_2S_3/In_2S_3 core/shell microspheres with enhanced photocatalytic activity. Sci Rep 4:4027

Zhuo S, Xu Y, Zhao W, Zhang J, Zhang B (2013) Hierarchical nanosheet-based MoS_2 nanotubes fabricated by an anion-exchange reaction of MoO_3-amine hybrid nanowires. Angew Chem Int Ed 52:8602–8606